



# Two-step Dropouts of Radiation Belt Electron Phase Space Density Induced by a Magnetic Cloud Event

Zhengyang Zou<sup>1</sup>, Pingbing Zuo<sup>1</sup>, Binbin Ni<sup>2</sup>, Zhonglei Gao<sup>1</sup>, Geng Wang<sup>1</sup>, Zhengyu Zhao<sup>1,2</sup>, Xueshang Feng<sup>1</sup>, and Fengsi Wei<sup>1</sup>

<sup>1</sup> Institute of Space Science and Applied Technology, Harbin Institute of Technology, Shenzhen, Shenzhen, Guangdong, People's Republic of China  
[pbzuo@hit.edu.cn](mailto:pbzuo@hit.edu.cn)

<sup>2</sup> Department of Space Physics, School of Electronic Information, Wuhan University, Wuhan, Hubei, People's Republic of China

Received 2020 January 28; revised 2020 May 7; accepted 2020 May 7; published 2020 May 26

## Abstract

We report a two-step dropout event of radiation belt electron phase space density (PSD) induced by a typical magnetic cloud (MC) that drove an intense geomagnetic storm. The first and second steps of PSD dropout occurred, respectively, in the initial and main phases of the storm with a short-time partial recovery between the two dropouts. In this event, the initial phase after the sudden commencement lasted for near 21 hr, which gives an ideal opportunity to investigate the nature of the radiation belt electron dropout by isolating the main phase from any losses occurring during the initial phase. Detailed analysis shows that the first step of the dropout in the initial phase is likely associated with the magnetopause shadowing effect in combination with ultra-low frequency wave-induced outward transport caused by sustaining enhanced dynamic pressure activity before the MC. Comparably, the prolonged strong southward interplanetary magnetic field inside the MC that resulted in the storm main phase is supposed to play an important role in the second step of significant electron losses to the interplanetary space. Additionally, the partial recovery of electron PSD between the two steps of the dropout is possibly due to the acceleration processes via wave-particle interactions with whistler-mode chorus waves. Our study demonstrated that persistently enhanced solar wind dynamic pressure, which is frequently observed inside interplanetary coronal mass ejections and corotating interaction regions, can play an important role in modulating the radiation belt electron dynamics before the storm main phase driven by these solar wind disturbances.

*Unified Astronomy Thesaurus concepts:* [Solar wind \(1534\)](#); [Solar-terrestrial interactions \(1473\)](#); [Astronomy data analysis \(1858\)](#)

## 1. Introduction

The Earth's magnetosphere is frequently influenced by magnetic storms or substorms driven by solar wind disturbances, such as interplanetary coronal mass ejections (ICMEs) or corotating interaction regions (CIRs), which can enhance, deplete, or barely change the population of radiation belt trapped particles on timescales from minutes to years (e.g., Li et al. 2001; Reeves et al. 2003; Baker et al. 2013; Thorne et al. 2013; Hajra et al. 2015; Ni et al. 2015; Su et al. 2015). One of the most remarkable and dramatic variations among them is radiation belt electron dropout, which is widely known as the rapid depletion of energetic electron fluxes or phase space density (PSD) in the outer radiation belt by one or more orders of magnitude in only a few hours or less (Morley et al. 2010; Tu et al. 2010; Turner et al. 2012a, 2012b, 2015; Yuan & Zong 2013; Turner & Ukhorskiy 2020).

Radiation belt electron dropout processes can be overall divided into two categories: (i) local loss into the Earth's atmosphere caused by wave-particle interactions with various plasma waves such as whistler-mode chorus, plasmaspheric hiss, and electromagnetic ion cyclotron (EMIC) waves (e.g., Summers et al. 2007; Thorne 2010; Yuan et al. 2012; Ni et al. 2013; Turner et al. 2014a, 2014b; Usanova et al. 2014; Ni et al. 2018; Medeiros et al. 2019); and (ii) loss to the interplanetary space on open drift shells via magnetopause shadowing combined with outward radial transport, which has a close relationship with the coupling between the solar wind and magnetosphere (Shprits et al. 2007; Turner et al. 2012a, 2012b, 2013, 2014a, 2014b; Kim & Lee 2014; Su et al. 2015; Turner & Ukhorskiy 2020). Dropout events

have been mostly reported as occurring during the storm main phase or right after the interplanetary (IP) shock, via the compression of the magnetopause, the sharp negative PSD gradient, or the ultra-low frequency (ULF) wave-caused outward diffusion (Shprits et al. 2017; Borovsky & Denton 2009; Ni et al. 2011; Hietala et al. 2014; Kilpua et al. 2015; Turner et al. 2012a, 2012b; Zhang et al. 2016; Hao et al. 2017; Turner & Ukhorskiy 2020). Note that all the above electron dropouts are regarded as appearing during the storm main phase with distinctly negative values of Dst. In these events, however, the storm main phase closely follows the IP shock in only a few minutes to hours, less than the one period of spacecraft orbit (e.g., Van Allen Probes with 9 hr, THEMIS with 15 hr). Therefore, it is hard to quantitatively compare the detailed evolutions of electron loss as well as the potential mechanisms before and during the storm main phase. It raises a question: could the electron dropout occur before the obvious decreasing of Dst, or could a typical dropout be divided into multiple steps in response to different stages of the geomagnetic storm? Recently, Katsavrias et al. (2015) reported a dropout event during a non-storm period on 2013 April 14 with persistently positive SymH caused by high solar wind dynamic pressure, showing clear evidence that the radiation belt electrons can rapidly loss to the magnetopause without the Dst effect.

In the present study, we select a particular MC-driven geomagnetic storm with an initial phase lasting for ~21 hr before the typical storm main phase. It provides an ideal opportunity to investigate the nature of the radiation belt electron dropout by isolating the main phase from any losses occurring during the initial phase after the storm sudden commencement (SSC), which is most often a very brief (few hours or less) period. In fact,

synthetically, a distinct two-step dropout of electron PSD is identified as occurring during this event, which to our knowledge has not been focused on previous studies. By comparing the electron PSD dropout characteristics during different stages of the storm in detail, we demonstrate the importance of sustaining high dynamic pressure before the main phase to the occurrence of radiation belt electron dropout, which is readily useful in future improvement of global simulations of radiation belt particle dynamics.

## 2. Data and Methodology

We use the electron pitch-angle resolved fluxes from the Relativistic Electron Proton Telescope (REPT) and the Magnetic Electron Ion Spectrometer (MagEIS) instruments (Baker et al. 2012; Blake et al. 2013) on board both Van Allen Probes (VAP; Mauk et al. 2012). To exclude the adiabatic changes and display the real electron loss, the electron fluxes are converted to PSD as a function of three adiabatic invariants (i.e.,  $\mu$ ,  $K$ , and  $L^*$ ) with the adoption of the TS04 geomagnetic field model (Tsyganenko & Sitnov 2005), by applying the method used in previous studies (e.g., Chen et al. 2005; Ni et al. 2009; Morley et al. 2013).

The data from Electric and Magnetic Field Instrument Suite Integrated Science (EMFISIS) instrumentation suite (Kletzing et al. 2013) on board both VAP are used to measure the ULF, ELF, and VLF waves. We also compare the spectra of the precipitated and trapped electron fluxes from the Medium Energy Proton/Electron Detector (MEPED) on board NOAA-POES 15, 16, 18, and 19 spacecraft during the electron dropout times. Also, the 1-minute-average solar wind plasma and magnetic field data, as well as geomagnetic indices, including SymH and AE, are downloaded from NASA/OMNI database. To identify the special solar wind disturbances, the magnetic field and plasma data are derived from the Magnetic and Field Investigation (MFI) and Solar Wind Experiment (SWE) instruments (Lepping et al. 1995; Ogilvie et al. 1995) on board the WIND spacecraft.

## 3. Observational Results

### 3.1. MC Event and the Driven Geomagnetic Storm

Figure 1 presents the solar wind magnetic field and plasma data from WIND and the simultaneous geomagnetic SymH index on 2013 June 27–29. During the interval between 03:29 UT on 28 June and 05:05 UT on 29 June, WIND observed a typical magnetic cloud. The magnetic cloud is identified based on several magnetic field and plasma signatures including strong magnetic fields (panel (a)), smooth rotation in the direction of magnetic fields (panels (c)–(d)), and exceptionally low proton temperature (panel (f)). An interplanetary shock was driven by this MC at 13:51 UT on 27 June (“S” label). Across the shock front, the magnitude of the magnetic field was notably enhanced, and the proton temperature, number density, and plasma bulk velocity also increased. Right at the leading edge of the magnetic cloud, a front boundary layer (MCBL) was formed as reported in previous studies (e.g., Wei et al. 2003a, 2003b, 2006; Zuo et al. 2006, 2007; Wang et al. 2010), with distinct features including that (1) the magnetic field sharply decreased and then recovered with larger field rotation like magnetic holes, (2) a dynamic pressure enhancement region appeared with maximum of  $P_{\text{dyn}} > 10$  nPa, which was attributed to the relatively high number density. The MCBL

was observed by WIND from 22:53 UT on 27 June to 03:29 UT on 28 June. It is expected that the magnetosphere was strongly compressed by this structure. Between the shock and the MCBL was the sheath region with relatively stronger turbulent magnetic fields. The SymH index in Figure 1(i) was almost constant near a negative value ( $-12$  nT, shown as the black horizontal dashed lines) until it suddenly increased at 14:54 UT on 2013 June 27, when the shock impinged on the magnetosphere and as a result the SSC was induced. Here we define the beginning of the storm main phase at the time when SymH recovered to the initial value ( $-12$  nT) and kept decreasing after that, i.e., 11:54 UT on 2013 June 28 (black vertical dashed line). The recovery phase of the storm began at 06:34 UT on 2013 June 29 (black vertical dashed line) when SymH arrived its minimum value ( $-111$  nT). In comparison to normal geomagnetic storms, during the storm initial phase closely followed by the SSC, the SymH in the present event maintained a positive value or fluctuated greater than the value before SSC ( $-12$  nT) for nearly 21 hr until a clear decrease indicating the start of the main phase. It gives us an ideal opportunity to analyze the detailed evolution of radiation belt electron distribution in response to different phases of the storm or different types of solar wind disturbances.

### 3.2. Two-step Electron PSD Dropout during the Pre-main and the Main Phase

Figure 2 shows an overview of the electron flux dropout during 2013 June 27–29. The whole event can be divided into two parts: the first dropout before the storm main phase and the subsequent enhanced dropout during the main phase. In the period between the IP shock and the storm main phase, both satellites observed an electron flux depletion at  $90^\circ$  pitch angles at higher  $L$ -shells for energies from 102 keV to 2.6 MeV (see Figures 2(c)–(i)). This depletion mainly occurred after more than one period of the spacecraft orbit, indicating that the IP shock should not be the primary loss process. The second dropout occurred during the storm main phase when the SymH index gradually decreased to less than  $-100$  nT accompanied by the AE increased to  $\sim 1000$  nT under the influence of the sustaining southward interplanetary magnetic field (IMF)  $B_z$ . Compared with the loss in the first step of the dropout, the electron fluxes during the second step of the dropout were depleted quickly down to the noise level at higher  $L$ -shells, and the visible dropout also penetrated to lower  $L$ -shells, indicative of a typical storm main phase dropout.

To exclude the adiabatic changes of electron fluxes, we show the temporal evolution of electron PSD versus  $L^*$  for relativistic electrons at  $\mu = 2290$  MeV/G (corresponding roughly to  $\sim 2.3$  MeV at  $L = 4.5$  or 3 MeV at  $L = 4.0$  for a dipole field) with  $K = 0.17 G^{1/2} R_E$  and  $K = 0.08 G^{1/2} R_E$  (corresponding to equatorial pitch angles of  $\sim 30^\circ$ – $40^\circ$  and  $50^\circ$ – $60^\circ$  for a dipole field) in Figures 3(a) and (b), respectively. When the IP shock arrived at 14:54 UT, VAP-B was located at  $L^* = 3.72$  in its inbound trajectory (curve 5), while VAP-A was at  $L^* = 3.77$  in its outbound trajectory (curve 6). Therefore, we briefly regard that the shock arrived between the time periods of curve 5 and curve 6 when investigating the PSD evolutions at  $L^* > 4$ . We also identify the time period of the arrival of MCBL as curves 10–12 and the beginning of the storm main phase as curve 16. In Figure 3(a), right after the shock (curve 6), the PSD experienced only a slight fluctuation by about 0.1 order at  $L^* > 4.5$ , suggesting that there were no rapid responses to the

## WIND MFI &amp; SWE (in GSE)

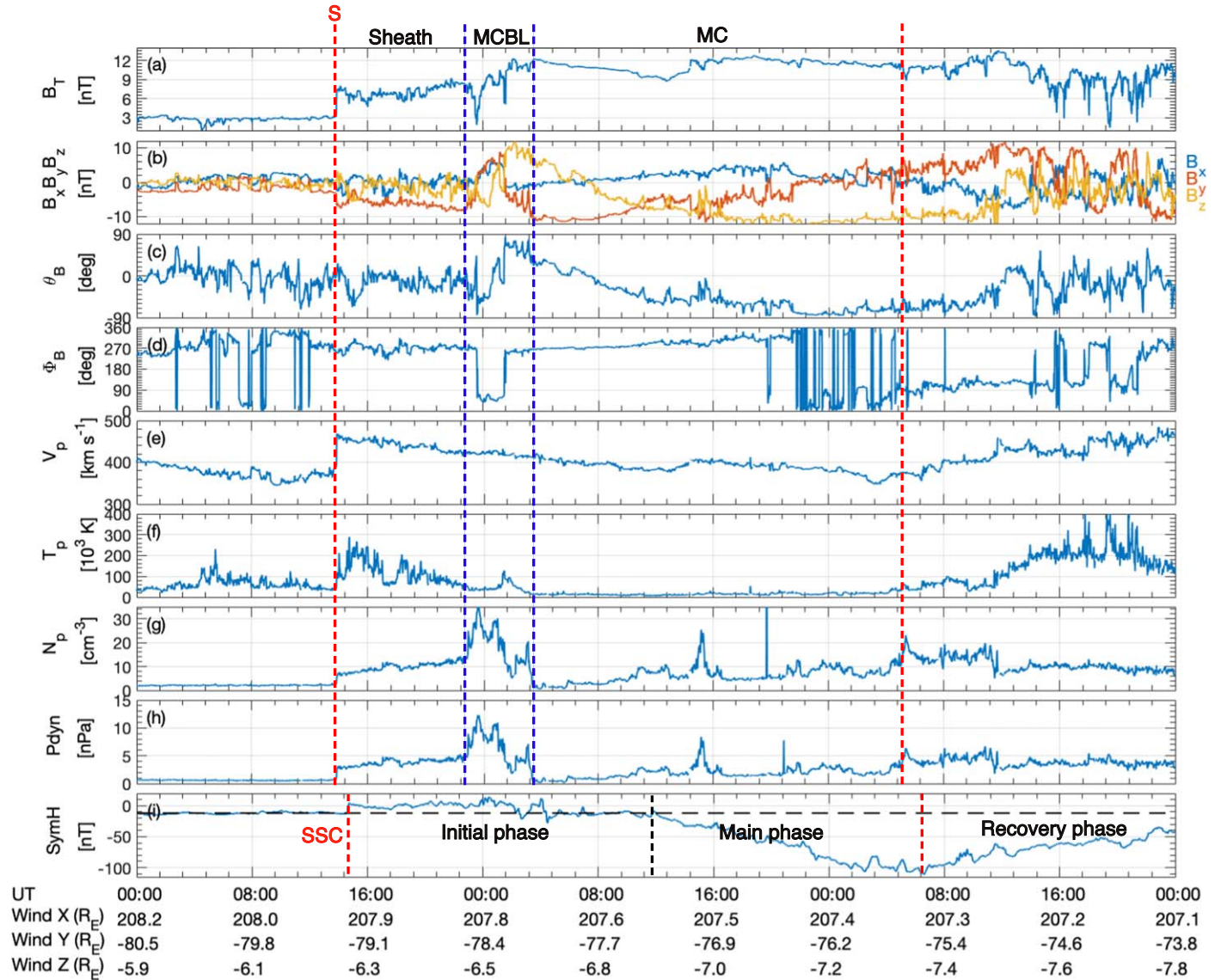


**Figure 1.** Overview of the magnetic cloud event from MFI and SWE on board WIND during 2013 June 27–29, including (a) magnetic field intensity, and (b) its three components (in GSE), (c) latitudinal angle and (d) longitudinal angle, (e) plasma bulk velocity, (f) proton temperature, (g) number density, (h) the solar wind dynamic pressure and (i) SymH index, respectively. The MC-induced interplanetary shock is marked with the first red vertical dashed line labeled by “S.” In panel (i), the start of the storm main phase is marked with the black vertical dashed line, and the averaged value of SymH before SSC is marked with the black horizontal dashed line. The different structures of MC disturbance, such as sheath region, MCBL and MC body, are referred to at the top of the figure.

IP shock. As the solar wind dynamic pressure maintained a high value corresponding to the passage of the sheath region, the PSD in the next three passes (curves 7–9) had an evident decrease at  $L^* > 5$ , especially for electrons at  $L^*$  from  $\sim 5.3$  to 5.9 where they had sharp drop by  $\sim 1$  to  $>2$  orders compared with the initial time (curves 1–6). The MCBL is a notable dynamic pressure enhancement region. When the MCBL impacted the magnetosphere, the PSD (curves 10–12) had been further depleted by about 0.5 orders compared to curve 9. After that, with the decrease of dynamic pressure after about 02:09 UT, the PSD decreased in a comparably smaller scale (curves 11–13) until they were accelerated to the initial level (curves 1–6) at  $L^* < \sim 4.3$ , as shown by curves 14–15. In the storm main phase, the PSD has a noticeable rapid loss at a broad spatial range ( $L^* > 3.5$ ), shown as curves 16–20. Because  $L$ -shells moved out to higher geophysical distance in the storm main phase, the apogee of VAP did not extend to as

high of  $L^*$  as it did in quiet periods. Therefore, the electron PSD at  $L^* > 4.6$  could not be obtained, as shown in the figures. However, the total change of the electron PSD at a broader range of  $L^*$  suggests a typical storm main phase dropout. The similar results can also be found in Figure 3(b), although curves 10, 12, and 19 are not shown due to the lack of the data above  $50^\circ$  pitch angles. Therefore, it is clearly identified that the two-step PSD dropout as well as the partial recovery between the two dropouts occurred in a broad range of pitch angles.

### 3.3. Comparison between the Two Steps of the Electron Dropout

To quantitatively compare the two steps of the dropout and analyze their potential generation mechanism(s), Figure 4 illustrates some parameters of solar wind and magnetic activity (Figures 4(a)–(b)), estimated minimum locations of the magnetopause (MP)



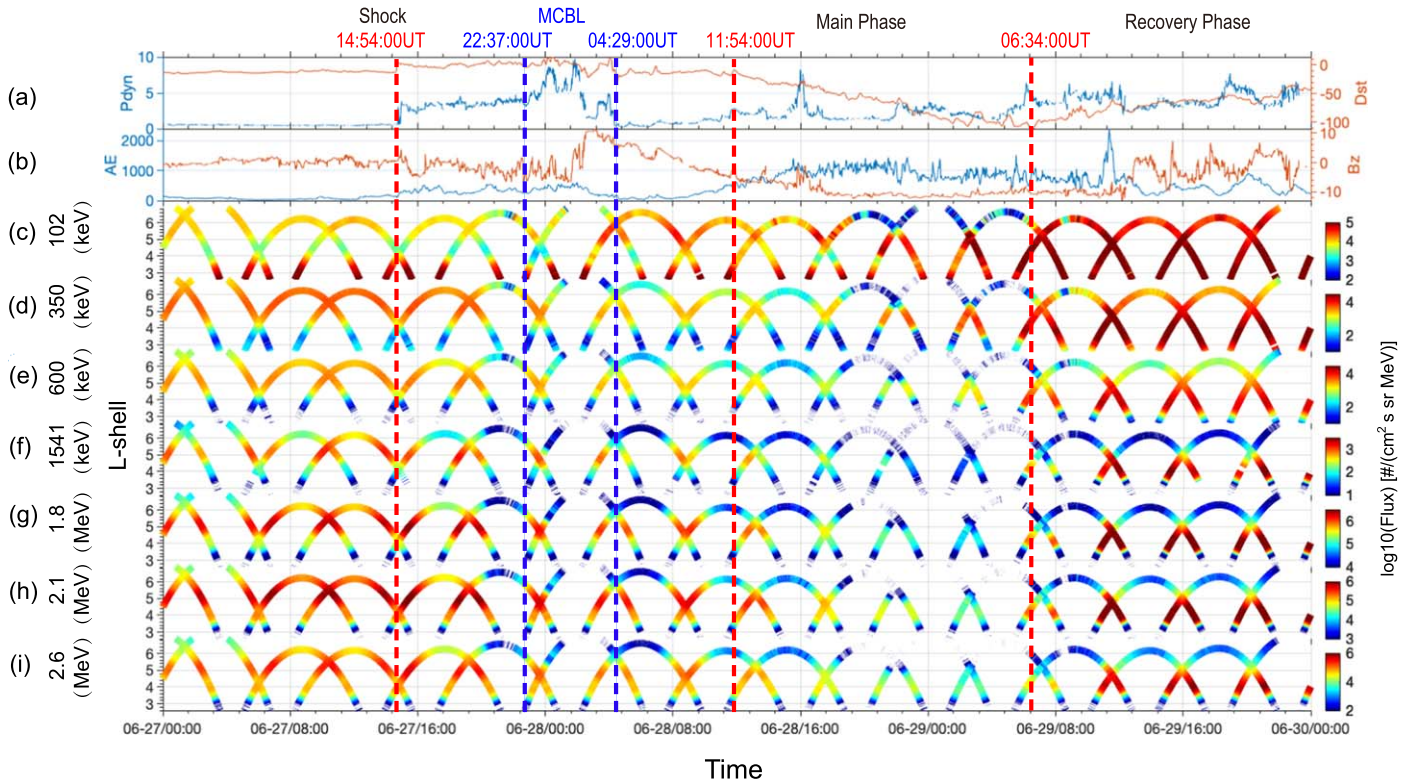


**Figure 2.** Overview of radiation belt electron dropout event during 2013 June 27–29: (a) the dynamic pressure (blue) and Dst (red); (b) AE, and IMF-Bz; (c)–(i) temporal evolutions of electron fluxes at 90° local observed pitch angle for seven specialized energies (from 102 keV to 2.6 MeV) at different  $L$ -shells measured by VAP -A and -B.

following Shue et al. (1997), and the last closed drift shell (LCDS) of relativistic electrons for  $K = 0.17$  (Figure 4(c)), the temporal evolution of electron PSD at  $\mu = 2290$  MeV/G with  $K = 0.17$  MeV/G (Figures 4(d)–(e)) and  $K = 0.08$  MeV/G (Figures 4(f)–(g)). The LANLGeoMag library is used to calculate LCDS (e.g., Albert et al. 2018), which had been regarded as a good indicator of the magnetopause shadowing (Xiang et al. 2017; Tu et al. 2019). In addition, the trapped and precipitating electron fluxes at  $>1$  MeV measured by NOAA-POES 15, 16, 18, and 19 spacecraft are also illustrated in Figures 4(h)–(i) to survey the atmospheric loss by wave-particle interactions. No significant changes at precipitating electron fluxes can be found in Figure 4(h), indicating that the electron dropout was hardly a result of local depletion to the atmosphere. By comparing the characteristics during both steps of the electron depletion, some apparent points can be reached. (1) Both steps of dropout were clearly sensitive to the MP as well as LCDS, strongly suggesting that the magnetopause shadowing effect plays a significant role in the entire electron dropout event. (2) In the first step of dropout, the LCDS moved to a lower location ( $L^* < 6$ ) during the passage of MCBL, which resulted in the continuous depletion of electron PSD. The possible reason can be that strong dynamic pressure within the MCBL led to further inward movement of the LCDS, and thus the loss via magnetopause shadowing could occur at lower  $L^*$ ; (3) Comparably, the storm main phase depletion appeared when the LCDS moved to lower  $L^*$  ( $L^* < 7$  or even to  $L^* = 5$ ), by the increase of the southward IMF-Bs and the growth of AE index from a few nT to  $>1000$  nT. In contrast, the magnetopause was compressed to comparable values ( $>8 R_E$ ), and the dynamic pressure was no more than 8 nPa. Consequently, the significant continuous southward IMF, rather than the high value of the dynamic pressure, could cause the further inward movement of

the LCDS, which potentially produces the electron loss on open drift shells (see Kim & Lee 2014).

Except for the global effects on the magnetospheric electron populations, the MC-induced storms or substorms could excite some plasma waves that potentially change the distributions of radiation belt electrons. We show the temporal evolutions of magnetic power spectral density (B-PSD) of waves from VAP at three specific frequency ranges, i.e., the ULF waves (at Pc-5 range: 1–5 mHz), the ELF waves (0–10 Hz), and the VLF waves (10–10000 Hz), respectively. Note that the wave data were only regularly measured in limited local time ranges by the spacecraft. So even if one kind of wave had not been observed, that does not mean there was no wave activity of these emissions existing on the same drift shell at other local times. First, in both steps of the dropout, the ULF waves at the Pc5 frequency range, which is comparable to the drift period of relativistic electrons (e.g., electrons at 1 MeV with drift period about 10 minutes), became remarkably intense. It means that the ULF wave-driven outward transport of electron can potentially rapidly deplete the electrons, especially at  $L^*$  less than the value of LCDS. Second, the EMIC waves, which are capable of precipitating high-energy radiation belt electrons to the atmosphere within  $<1$  hr, were hardly identified in Figures 5(c)–(d) by both spacecraft. Although we cannot exclude the existence of EMIC waves at on the same drift shell on other local times, the absence of the obvious local minimum of the electron PSD during both steps of the dropout (see curves 09–13, 17–20 in Figures 3(a)–(b)) suggests that EMIC-induced resonant scattering could not be the main mechanism to rapidly deplete the relativistic electron (see Aseev et al. 2017; Shprits et al. 2007). Third, the chorus waves (marked in Figure 5(e)), which can potentially accelerate the relativistic

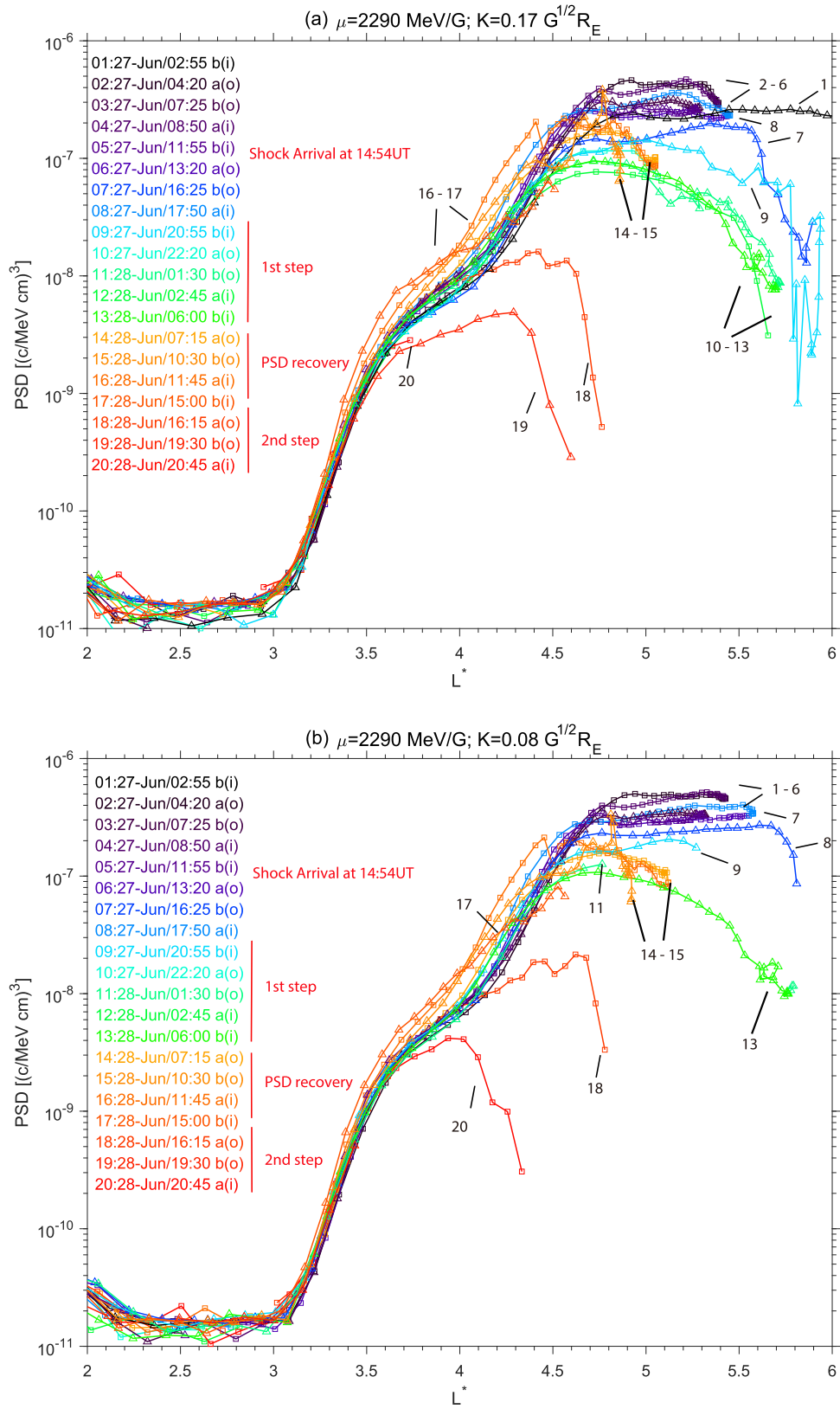


**Figure 3.** Relativistic electron PSD distributions as a function of  $L^*$  for fixed  $\mu = 2290 \text{ MeV/G}$  and selected two  $K$ : (a)  $K = 0.17 \text{ G}^{1/2} R_E$ , (b)  $K = 0.08 \text{ G}^{1/2} R_E$ . Various colors correspond to different inbound or outbound orbit passes from VAP-A (squares) and VAP-B (triangles), with the start time of each pass (o: outbound; i: inbound) labeled. Each curve is numbered for ease of identification.

electron and form the PSD peak at the heart of the outer radiation belt (e.g., Horne et al. 2005; Thorne et al. 2013), were clearly observed by VAP-A from 11:53 UT to 14:05 UT at

$L = 5.8$  to  $L = 4.5$ . The time interval and spatial coverage are in accordance with the partial recovery of electron PSD, indicating that local electron acceleration driven by chorus can



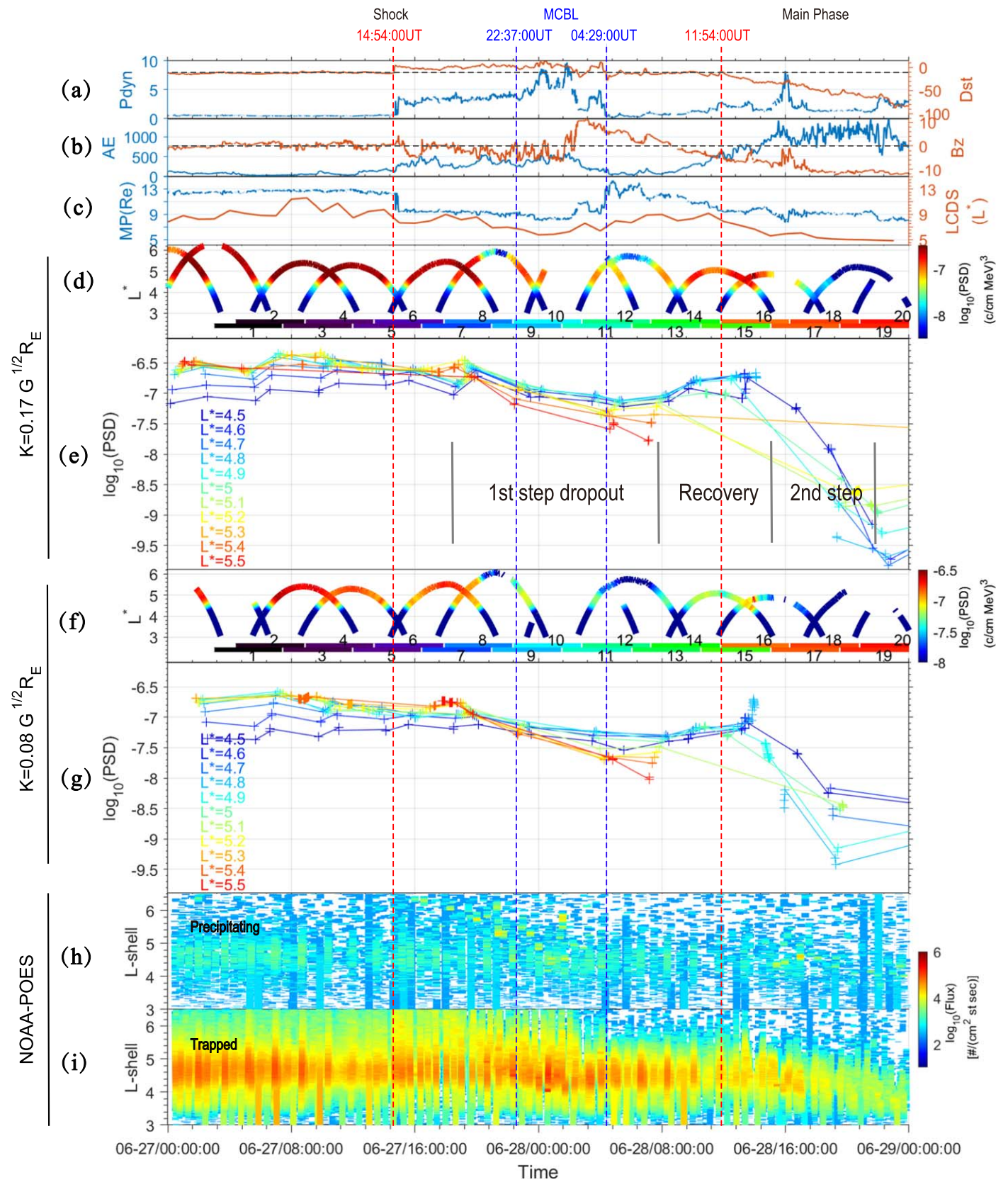


**Figure 4.** Temporal evolutions of electron PSD distributions during 2013 June 27–29: (a)–(b)  $P_{\text{dyn}}$ ,  $Dst$ ,  $AE$ , and  $IMF-Bz$ ; (c) magnetopause location ( $MP$ ) and  $LCDS$ ; (d) electron PSD vs.  $L^*$  and (e) color-coded temporal evolution of electron PSD at  $K = 0.17 G^{1/2} R_E$  and  $\mu = 2290 \text{ MeV/G}$  (the inbound and outbound passes are marked as in Figure 3); (f) electron PSD vs.  $L^*$  and (g) color-coded temporal evolution of electron PSD at  $K = 0.08 G^{1/2} R_E$  and  $\mu = 2290 \text{ MeV/G}$ ; and (h)–(i) spectra of precipitating and trapped electron flux from NOAA-POES 15, 16, 18, and 19 at  $E_k > 1 \text{ MeV}$ .

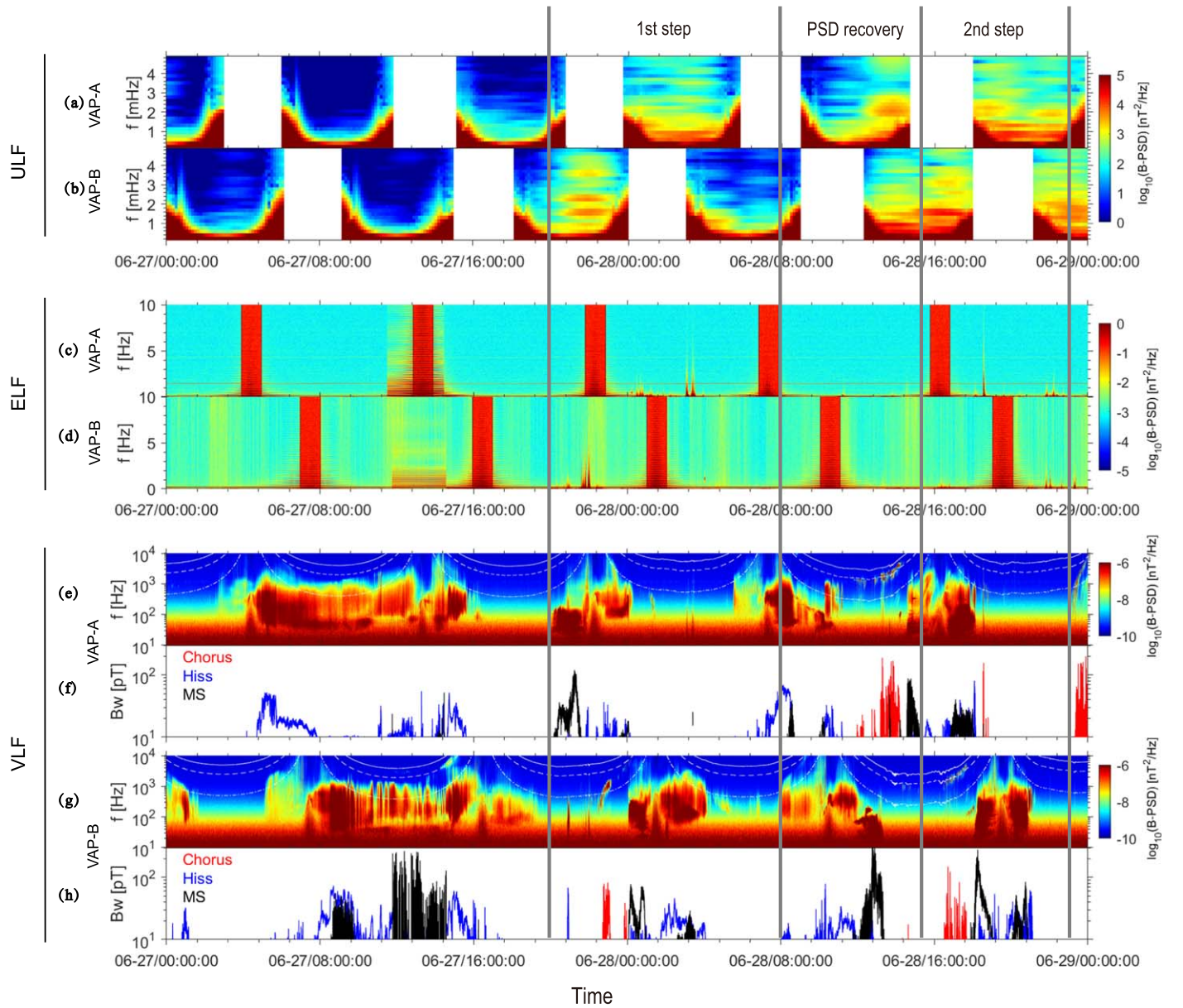


**Figure 5.** Temporal evolutions of the magnetic power spectral density (B-PSD) of (a)–(b) ULF waves at 1–5 mHz; (c)–(d) ELF waves at 0–10 Hz; and (e) and (g) VLF waves at  $10^1$ – $10^4$  Hz as well as (f) and (h) the amplitude ( $B_w$ ) of the identified whistler-mode chorus (red), plasmaspheric hiss (blue), and magnetosonic (MS) waves (black) observed from VAP-A and VAP-B, respectively.

contribute largely to the observations of electron PSD growth. In addition, VAP-B also captured the waves when arriving at a similar spatial position after about 4 hr when the electron PSD had arrived at their second step of the dropout. After the second step of the dropout, the chorus waves were also observed by VAP-A with  $B_w > 100$  pT along with the PSD growth, which is beyond the scope of our current study. In addition, the plasmaspheric hiss (blue) and MS waves (black) were also present during this event. However, both waves can hardly deplete relativistic radiation belt electrons within a few hours (e.g., Bortnik & Thorne 2010; Ripoll et al. 2016).

#### 4. Summary and Discussion

In this investigation, we report and discuss a two-step electron PSD dropout event. The first and second step of the dropout occurred during the initial phase after the SSC and during the

main phase of an MC-induced geomagnetic storm, respectively. The results show that the main phase dropout was more pronounced than the loss in the initial phase. However, the persistence of the strong dynamic pressure in the sheath region before the storm main phase cannot be neglected because their possible capabilities (as well as the ULF-induced outward transport) to generate the electron PSD dropout without the Dst effect. Moreover, it cannot be ignored that the sharp negative gradient of the PSD at higher  $L^*$  after the initial phase dropout may potentially strengthen the rapid loss of the electrons in the main phase by radial diffusions (e.g., Turner et al. 2012a, 2014a, 2014b). The further depletion of the electron PSD in the first step was highly relative to the exceptional enhancement of dynamic pressure within the MCBL. It gives evidence that MCBL could potentially influence the dynamics of radiation belt electrons, which has not drawn much attention. Actually, the MCBL structure could also be identified as being



partly responsible for the electron dropout event in Katsavrias et al. (2015), although it had not been pointed out in that paper. A further statistical study needs to be carried out to investigate the essential role of MCBL in driving the acceleration and depletion of radiation belt trapped particles.


The conclusions are summarized as follows.

- (1) The persistently enhanced solar wind dynamic pressure after SSC, which is frequently observed inside ICMEs and CIRs, can play an important role in modulating radiation belt electron dynamics by solar wind-magnetosphere coupling.
- (2) With more enhanced dynamic pressure, the MCBL in the ICMEs could potentially deplete the radiation belt electrons to the interplanetary space by moving their last closed drift shell further inward.
- (3) The whistler-mode chorus waves can potentially weaken the dropout by accelerating the relativistic electrons, while ULF waves may essentially strengthen the dropout by leading the outward transport of the radiation belt electrons.

This work was supported by the NSFC grants 41731067, 41674163, the Guangdong Basic and Applied Basic Research Foundation (grant No. 2019A1515011067), the B-type Strategic Priority Program of the Chinese Academy of Sciences (grant No. XDB41000000), and the Shenzhen Technology Project (grant No. JCYJ20180306171748011). The Wind MFI and SWE data and geomagnetic indices are available from the NASA OmniWeb (<http://cdaweb.gsfc.nasa.gov>). The REPT and MagEIS data are obtained from <https://spdf.gsfc.nasa.gov/pub/data/rbsp>. The EMFISIS data are derived from <https://emfisis.physics.uiowa.edu/data/index>. The NOAA-POES data are from <https://spdf.gsfc.nasa.gov/pub/data/noaa/>.

### ORCID iDs


Zhengyang Zou  <https://orcid.org/0000-0003-1273-4573>

Pingbing Zuo  <https://orcid.org/0000-0003-4711-0306>

Binbin Ni  <https://orcid.org/0000-0001-6644-0728>

Zhonglei Gao  <https://orcid.org/0000-0001-7397-930X>

Geng Wang  <https://orcid.org/0000-0003-4464-429X>

Xueshang Feng  <https://orcid.org/0000-0001-8605-2159>

### References

Albert, J. M., Selesnick, R. S., Morley, S. K., Henderson, M. G., & Kellerman, A. C. 2018, *JGRA*, **123**, 9597

Aseev, N. A., Shprits, Y. Y., Drozdov, A. Y., et al. 2017, *JGRA*, **122**, 10102

Baker, D. N., Kanekal, S. G., Hoxie, V. C., et al. 2012, *SSRv*, **179**, 337

Baker, D. N., Kanekal, S. G., Hoxie, V. C., et al. 2013, *Sci*, **340**, 186

Blake, J. B., Carranza, P. A., Claudepierre, S. G., et al. 2013, *SSRv*, **179**, 383

Borovsky, J. E., & Denton, M. H. 2009, *JGRA*, **114**, A02201

Bortnik, J., & Thorne, R. M. 2010, *JGRA*, **115**, A07213

Chen, Y., Friedel, R. H. W., Reeves, G. D., Onsager, T. G., & Thomsen, M. F. 2005, *JGRA*, **110**, A10210

Hajra, R., Tsurutani, B. T., Echer, E., et al. 2015, *ApJ*, **799**, 39

Hao, Y., Zong, Q. -G., Zhou, X. -Z., et al. 2017, *GeoRL*, **44**, 7618

Hietala, H., Kilpua, E. K. J., Turner, D. L., & Angelopoulos, V. 2014, *GeoRL*, **41**, 2258

Home, R. B., Thorne, R. M., Glauert, S. A., et al. 2005, *JGRA*, **110**, A03225

Katsavrias, C., Daglis, I. A., Turner, D. L., et al. 2015, *GeoRL*, **42**, 10521

Kilpua, E. K. J., Hietala, H., Turner, D. L., et al. 2015, *GeoRL*, **42**, 3076

Kim, K.-C., & Lee, D.-Y. 2014, *JGRA*, **119**, 5495

Kletzing, C. A., Kurth, W. S., Acuna, M., et al. 2013, *SSRv*, **179**, 127

Lepping, R. P., Acuna, M. H., Burlaga, L. F., et al. 1995, *SSRv*, **71**, 207

Li, X., Baker, D. N., Kanekal, S. G., Looper, M., & Temerin, M. 2001, *GeoRL*, **28**, 3827

Liu, Z. Y., Zong, Q.-G., Zhou, X.-Z., Ma, X. H., & Liu, T. 2017, *JGRA*, **122**, 8037

Mauk, B. H., Fox, N. J., Kanekal, S. G., et al. 2012, *SSRv*, **179**, 3

Medeiros, C., Souza, V. M., Vieira, L. E. A., et al. 2019, *ApJ*, **872**, 36

Morley, S. K., Friedel, R. H. W., Spanswick, E. L., et al. 2010, *GeoRL*, **37**, 06102

Ni, B., Bortnik, J., Thorne, R. M., Ma, Q., & Chen, L. 2013, *JGRA*, **118**, 7740

Ni, B., Shprits, Y., Hartinger, M., et al. 2011, *JGRA*, **116**, A03208

Ni, B., Shprits, Y., Nagai, T., et al. 2009, *JGRA*, **114**, A05208

Ni, B., Zou, Z., Fu, S., et al. 2018, *GeoRL*, **45**, 1228

Ni, B., Zou, Z., Gu, X., et al. 2015, *JGRA*, **120**, 4863

Ogilvie, K. W., Chornay, D. J., Fritzenreiter, R. J., et al. 1995, *SSRv*, **71**, 55

Reeves, G. D., McAdams, K. L., Friedel, R. H. W., & O'Brien, T. P. 2003, *GeoRL*, **30**, 1529

Ripoll, J.-F., Reeves, G. D., Cunningham, G. S., et al. 2016, *GeoRL*, **43**, 5616

Shprits, Y. Y., Daae, M., & Ni, B. 2012, *JGRA*, **117**, A01219

Shprits, Y. Y., Kellerman, A. C., Aseev, N. A., Drozdov, A. Y., & Michaelis, I. 2017, *GeoRL*, **44**, 1204

Shprits, Y. Y., Meredith, N. P., & Thorne, R. M. 2007, *GeoRL*, **34**, L11110

Shue, J.-H., Chao, J. K., Fu, H. C., et al. 1997, *JGR*, **102**, 9497

Su, Z., Zhu, H., Xiao, F., et al. 2015, *NatCo*, **6**, 10096

Summers, D., Ni, B., & Meredith, N. P. 2007, *JGRA*, **112**, A04206

Thorne, R. M. 2010, *GeoRL*, **37**, L22107

Thorne, R. M., Li, W., Ni, B., et al. 2013, *Natur*, **504**, 411

Tsyganenko, N. A., & Sitnov, M. I. 2005, *JGRA*, **110**, A03208

Tu, W., Selesnick, R., Li, X., & Looper, M. 2010, *JGRA*, **115**, A07210

Tu, W., Xiang, Z., & Morley, S. K. 2019, *GeoRL*, **46**, 9388

Turner, D. L., Angelopoulos, V., Li, W., et al. 2013, *JGRA*, **118**, 2196

Turner, D. L., Angelopoulos, V., Li, W., et al. 2014a, *JGRA*, **119**, 1960

Turner, D. L., Angelopoulos, V., Morley, S. K., et al. 2014b, *JGRA*, **119**, 1530

Turner, D. L., Morley, S. K., Miyoshi, Y., Ni, B., & Huang, C. -L. 2012a, in *Dynamics of the Earth's Radiation Belts and Inner Magnetosphere*, Geophysical Monograph Series, Vol. 199, ed. D. Summers et al. (Washington, DC: AGU), 195

Turner, D. L., O'Brien, T. P., Fennell, J. F., et al. 2015, *GeoRL*, **42**, 9176

Turner, D. L., Shprits, Y. Y., Hartinger, M., & Angelopoulos, V. 2012b, *NatPh*, **8**, 208

Turner, D. L., & Ukhorskiy, A. Y. 2020, in *The Dynamic Loss of Earth's Radiation Belts*, ed. A. N. Jaynes & M. E. Usanova (Amsterdam: Elsevier), 1

Usanova, M. E., Drozdov, A., Orlova, K., et al. 2014, *GeoRL*, **41**, 1375

Wang, Y., Wei, F., Feng, X., et al. 2010, *PhRvL*, **105**, 195007

Wei, F., Feng, X., Yang, F., & Zhong, D. 2006, *JGRA*, **111**, A03102

Wei, F., Luo, R., Fan, Q., & Feng, X. 2003a, *JGRA*, **108**, 1263

Wei, F., Luo, R., Fan, Q., Zhong, D., & Feng, X. 2003b, *GeoRL*, **30**, 2283

Xiang, Z., Tu, W., Li, X., et al. 2017, *JGRA*, **122**, 9858

Yuan, C., & Zong, Q. 2013, *JGRA*, **118**, 7545

Yuan, Z., Xiong, Y., Wang, D., et al. 2012, *JGRA*, **117**, A08324

Zhang, X.-J., Li, W., Thorne, R. M., et al. 2016, *JGRA*, **121**, 8300

Zuo, P., Wei, F., & Feng, X. 2006, *GeoRL*, **33**, L15107

Zuo, P., Wei, F., & Feng, X. 2007, *SoPh*, **242**, 167

Zuo, P., Wei, F., Feng, X., Xu, X., & Song, W. 2007, *JGRA*, **115**, A10102